Copper-Containing Magnesioferrite in Vesicular Trachyandesite in a Lava Tube from the 2012-2013 Eruption of the Tolbachik Volcano, Kamchatka, Russia

Sharygin, Victor V.

MDPI
2018-11

Sharygin, V V, Kamenetsky, V S, Zhitova, L M, Belousov, A B & Abersteiner, A 2018, 'Copper-Containing Magnesioferrite in Vesicular Trachyandesite in a Lava Tube from the 2012-2013 Eruption of the Tolbachik Volcano, Kamchatka, Russia', Minerals, vol. 8, no. 11, 514. https://doi.org/10.3390/min8110514

http://hdl.handle.net/10138/326102
10.3390/min8110514

minerals

MDPI

Article

Copper-Containing Magnesioferrite in Vesicular Trachyandesite in a Lava Tube from the 2012–2013 Eruption of the Tolbachik Volcano, Kamchatka, Russia

Victor V. Sharygin [1,2,3,*], Vadim S. Kamenetsky [4,5], Liudmila M. Zhitova [1,2], Alexander B. Belousov [6] and Adam Abersteiner [5]

1 V.S. Sobolev Institute of Geology and Mineralogy, Novosibirsk 630090, Russia; zhitova@igm.nsc.ru
2 Department of Geology and Geophysics, Novosibirsk State University, Novosibirsk 630090, Russia
3 Institute of Physics and Technology, Ural Federal University, Ekaterinburg 620002, Russia
4 Institute of Experimental Mineralogy, Chernogolovka 142432, Russia; Dima.Kamenetsky@utas.edu.au
5 School of Natural Sciences, University of Tasmania, Hobart, TAS 7001, Australia; adam.abersteiner@utas.edu.au
6 Institute of Volcanology and Seismology, Petropavlovsk-Kamchatsky 683006, Russia; belousov@mail.ru
* Correspondence: sharygin@igm.nsc.ru; Tel.: +7-383-330-80-84

Received: 13 October 2018; Accepted: 5 November 2018; Published: 8 November 2018

Abstract: Cu-rich magnesioferrite was found in vesicular basaltic trachyandesite in one of lava tubes (Duplex) that formed during the 2012–2013 eruption of the Tolbachik volcano, Kamchatka. This mineral is commonly associated with hematite, tenorite, halite, sylvite, and Ca-rich silicates (mainly, esseneite and Na-rich melilite) in high-temperature (800–1000 °C) reactionary zones (up to 100 μm) covering vesicular rocks and lava stalactites in the Duplex tube. The mineral relationships of this assemblage indicate the following crystallization sequence: Ca-rich silicates + hematite → Cu-rich magnesioferrite → tenorite → chlorides. This formed due to the reaction of hot gases containing Cu, alkalis, and Cl with solidified lava rock. The composition of magnesioferrite varies strongly in CuO (5.8–17.3 wt %; cuprospinel end-member—15–47 mol %), whereas the contents of other oxides are minor, indicating the main isomorphic substitution is $Mg^{2+} \leftrightarrow Cu^{2+}$. Compositions with maximal CuO content nominally belong to Mg-rich cuprospinel: $(Cu_{0.48}Mg_{0.41}Mn_{0.09}Zn_{0.02}Ca_{0.02})(Fe^{3+}{}_{1.94}Al_{0.03}Ti_{0.02})O_4$. Increasing CuO content of the Duplex Cu-rich magnesioferrite is reflected in Raman spectra by moderate right shifting bands at ≈700–710 and 200–210 cm^{-1} and the appearance of an additional band at 596 cm^{-1}. This supports the main isomorphic scheme and may indicate a degree of inversion in the spinel structure.

Keywords: magnesioferrite; cuprospinel; hematite; tenorite; trachyandesite; lava tube; Tolbachik volcano; Kamchatka

1. Introduction

Copper-rich spinels are well-documented in synthetic compounds, but rarely occur as minerals in the natural environment. Their origin is largely attributed to combustion processes or fumarole activity in young volcanoes. Cuprospinel, $CuFe^{3+}{}_2O_4$, was first described as a new mineral species from burnt dump from the Consolidated Rambler Mines Limited near Baie Verte, Newfoundland, Canada [1]. In this semi-anthropogenic system, cuprospinel is associated with Cu-rich magnesioferrite (13.9 wt % CuO) and hematite. This assemblage was formed as a result of a spontaneous ignition and burning of the mined copper–zinc ore. Cuprospinel, together with delafossite ($CuFeO_2$), tenorite, and Fe-silicates,

were found as products of oxidative combustion of copper sulfides and related phases (hematite, quartz, and K-silicates), along with an additional silica flux found at the Olympic Dam copper smelter [2]. A new Cu-rich spinel, thermaerogenite ($CuAl_2O_4$; IMA 2018-021), cuprospinel, and other Cu-bearing spinel-group minerals (usually with >6 wt % CuO: gahnite, spinel, and magnesioferrite) were recently discovered in the Arsenatnaya fumarole, which occurs in the Second scoria cone of the Northern Breakthrough of the 1975–1976 Great Tolbachik Fissure Eruption, Tolbachik volcano, Kamchatka, Russia [3–5] and in the Western paleo-fumarole field at Mountain 1004, ancient eruption of Tolbachik (≈2000 years) [5]. In this paper, we present detailed descriptions of a new locality for Cu-bearing magnesioferrite within the Tolbachik volcanic system, where it occurs as exhalation products in basaltic trachyandesites from the Duplex lava tube of the 2012–2013 flank fissure eruption. The findings of new Cu-rich spinels provide new insights into a new Cu-dominant clan within the spinel supergroup [6].

2. Brief Data of the 2012–2013 Fissure Eruption of the Tolbachik Volcano

The 2012–2013 flank fissure eruption of the Tolbachik volcano in the Kamchatka Peninsula (Far East, Russia) lasted 9 months and produced 0.54 km^3 of basaltic trachyandesite lava that covered a total area of 36 km^2 with a maximum thickness of 70 m [7] (Figure 1). This eruption is considered as one of the most voluminous historical outpouring of basic lava in a subduction-related environment. During the eruption, the style of lava propagation gradually changed from channel-fed 'a'a flows to tube-fed pahoehoe flows [8]. When the rate of magma discharge declined from the initial 440 m^3/s to several tens of m^3/s in January 2013, lava tubes started forming via surface solidification ("roofing") of the open lava channels (Figure 2A). During the later stages of the eruption, the tube system extended downslope by complex branching to reach a total length of ≈4 km and included multiple interlacing tubes with average diameters ranging from 1 to 10 m.

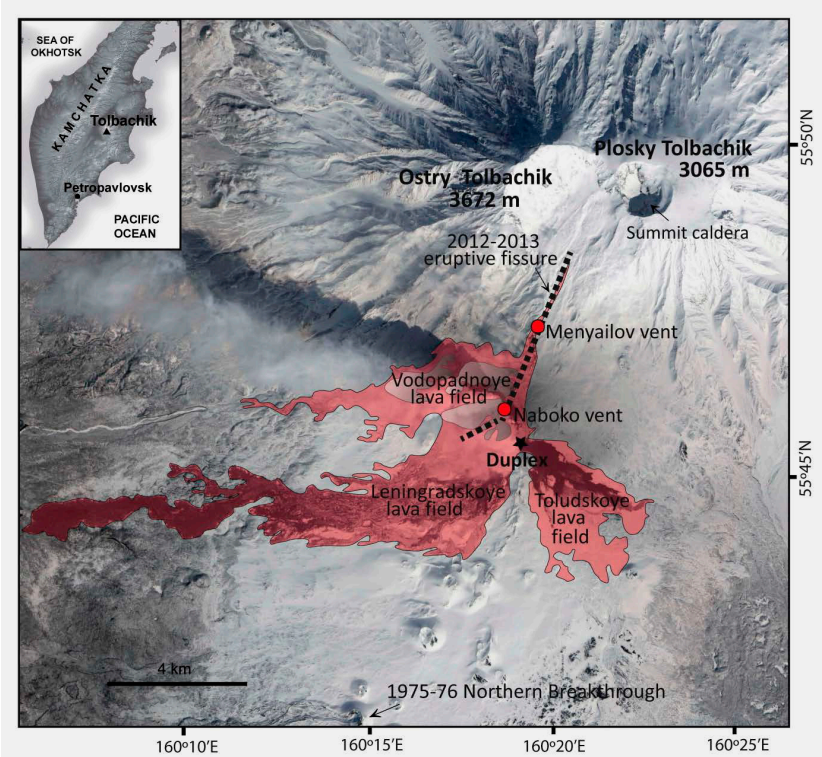

Figure 1. Sketch map after References [8,9] showing the distribution of the 2012–2013 Tolbachik eruption lava fields, fissures, vents, and the location of the Duplex lava tube segment (sampling site). The map is derived from TERRA, ASTER (NASA, JPL), and EO-1 ALI (NASA) satellite image interpretations and field observations. The topographic base is a DEM-derived from SRTM X-band (DLR).

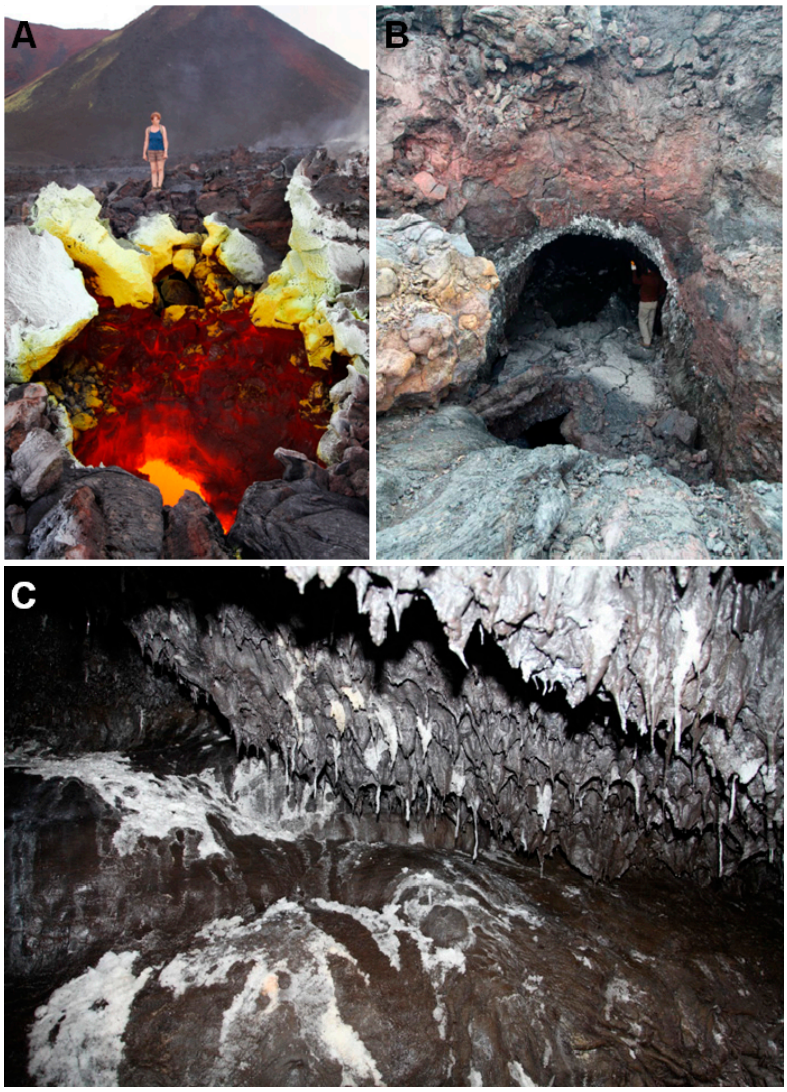

Figure 2. (**A**) Gas-venting skylight in the lava tube during the Tolbachik eruption in 2012–2013. (**B**) Entrance into the Duplex lava tube after the 2012–2013 eruption, June 2017. (**C**) Lava "stalactites" covered with chlorides on the roof of the Duplex tube, June 2017.

Lava flowing through the tube system preserved temperatures and viscosities close to those in the source (1082 °C and $(1-3) \times 10^3$ Pa·s) [8], but experienced degassing, which was frequently observed as bursting bubbles at the lava surface. Gases released from the lava leaked upwards through the fractured roof of the tubes as well as vigorously vented out through "skylights" (Figure 2A). The temperature of venting gases was measured directly at the skylights [10,11] and recorded temperatures as high as the lava (1025–1065 °C). The high temperatures of the volcanic gases were probably caused by mixing with air through skylights and associated oxidation, which triggered partial melting of the roof rocks and formation of numerous lava stalactites (Figure 2C).

Rocks in the areas of gas venting (skylights and open cracks) were covered by colorful crusts composed of various minerals precipitated from the gas phase [12–15]. The green-colored encrustations are largely composed of chlorides and complex K-Cu-sulfates, most notably cyanochroite ($K_2Cu(SO_4)_2 \cdot 6H_2O$). Other minerals include gold, anglesite ($PbSO_4$), unidentified Cu_2FeBO_5 and Ag_2S minerals, hematite, and galena [12]. A new mineral, belomarinaite ($KNaSO_4$), was discovered in sublimates of the skylight shown in Figure 2A [15]. Some sublimate spots (small fumaroles) contain fedotovite ($K_2Cu_3O(SO_4)_3$), euchlorine ($KNaCu_3O(SO_4)_3$), parawulffite ($K_5Na_3Cu_8O_4(SO_4)_8$), an unidentified $KNaCu_2O(SO_4)_2$ phase, chalcocyanite, aphthitalite, ralstonite,

chalcantite, erythrosiderite, and eriochalcite [14,16]. Large fumaroles of the 2012–2013 Tolbachik fissure eruption (e.g., Saranchinaitovaya fumarole, Naboko scoria cone) contain mineral assemblages comparable with fumaroles from the First and Second scoria cones of the Northern Breakthrough of the Great Tolbachik Fissure eruption (1975–1976), but shows poorer mineral diversity and abundance. Nevertheless, five new sulfate mineral species were recently discovered in the sublimates of the Saranchinaitovaya fumarole: itelmenite $Na_4Mg_3Cu_3(SO_4)_8$ [17], ivsite $Na_3H(SO_4)_2$ [18], bubnovaite $K_2Na_8Ca(SO_4)_6$ [19], hermannjahnite $CuZn(SO_4)_2$ [20], and saranchinaite $Na_2Cu(SO_4)_2$ [21]. Other minerals are represented by anhydrite, chalcocyanite, euchlorine, thénardite, aphthitalite and hematite [20,21].

Towards the cessation of the eruption, the tube system became separated by plugs of solidified lava, creating numerous isolated segments that started to cool from ≈1000 °C independently from each other. Segments with intensive air inflow through their entrances cooled down to ambient temperatures within a year, whereas segments with gas outflow still had elevated temperatures in 2017. For example, segment "Sushilka" (meaning "Dryer" in Russian) cooled to 20 °C by mid-2015, then the temperature abruptly increased to 100–150 °C and remained at this level (last measurement in August 2017), because the air circulation reversed back from gas inflow to gas outflow.

The studied tube "Dvoinaya" (meaning "Duplex" in Russian; 55°45′28″ N, 160°19′24.6″ E) is represented by two galleries located one above the other and consists of a 150 m-long segment of the lava tube system that was cut-off from the lava supply in May 2013. Since then, the tube (that originally had air outflow from its entrance) started to cool and became accessible in 2017 (Figure 2B,C). Very complex distributions of temperatures were recorded in the upper gallery: ≈50 °C in the entrance area, whereas the walls inside the tube had strong temperature gradients from 100 °C and up to 540 °C in some wall fractures [2]. The entrance to the lower inaccessible gallery of this tube segment recorded air temperatures around 200 °C. It is noteworthy that at the same time, the incandescent cracks at the surface of the lava field (≈100 m from the tube entrance) were as hot as 660 °C. The interior of the recently-cooled parts of lava tubes, especially around wall fractures, is coated by a fine-grained, grayish-white material. The mineral assemblage, covering the vesicular rocks and stalactites in the Duplex tube (Figure 2C), mainly consists of intergrowths of Na-K-chlorides and tenorite (CuO), magnesioferrite, hematite, and newly-formed Ca-Fe-rich silicates [2]. These rocks are currently being studied at the time of this present work (Figure 3). It is noteworthy that field observations of the Duplex tube in 2018 showed an absence of visible chlorides on stalactites due to infiltrating rain water.

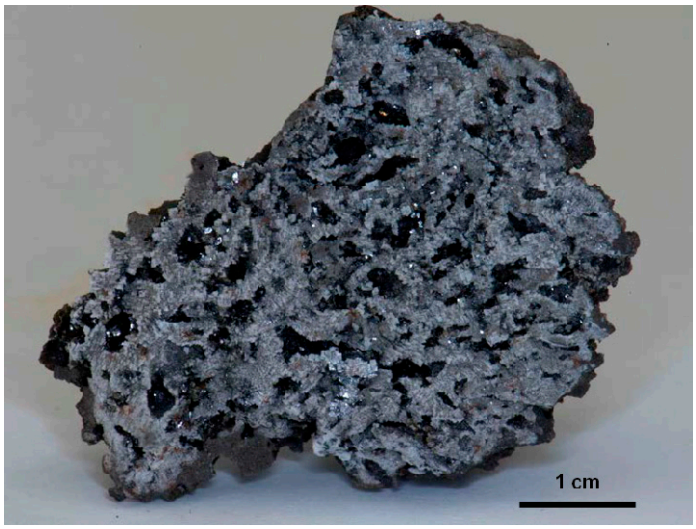

Figure 3. General view of sample from the lava wall covering by crystals of chlorides and tenorite, Duplex lava tube.

3. Analytical Methods

Double-polished rock sections (≈50 μm in thickness) and polished rock fragments mounted in epoxy resin were used for transmitted and reflected light microscope examination of the Duplex basaltic trachyandesite rock with chloride coatings (Figure 3). During the preparation of polished samples, no water-bearing abrasives were used. Identification of minerals was based on energy-dispersive spectra (EDS), back-scattered electron (BSE) images, and elemental mapping (EDS system), using a TESCAN MIRA 3MLU scanning electron microscope equipped with an INCA Energy 450 XMax 80 microanalysis system (Oxford Instruments Ltd., Abingdon, UK) at the V.S. Sobolev Institute of Geology and Mineralogy (IGM), Novosibirsk, Russia. The instruments were operated at an accelerating voltage of 20 kV and a probe current of 1 nA in high-vacuum modes. An EDS quantitative analyses of minerals were done using TESCAN MIRA 3MLU scanning electron microscope at an accelerating voltage of 20 kV, a probe current of 1 nA, and an accumulation time of 20 s. The following simple compounds and metals were used as reference standards for most of the elements: SiO_2 (Si and O), Al_2O_3 (Al), diopside (Mg and Ca), albite (Na), orthoclase (K), $Ca_2P_2O_7$ (P), BaF_2 (Ba and F), Cr_2O_3 (Cr), $CsRe_2Cl_6$ (Cl), $LaPO_4$ (La), $CePO_4$ (Ce), SrF_2 (Sr), and metallic Ti, Fe, Mn, Zn, Ni, V, and Cu. Correction for matrix effects was done using the XPP algorithm, implemented in the software of the microanalysis system. Metallic cobalt served for quantitative optimization (normalization to probe current and energy calibration of the spectrometer).

Electron microprobe analyses (EMPA) in wavelength-dispersive (WDS) mode were performed for rock-forming and opaque minerals from the Tolbachik rocks using a JXA-8100 microprobe (Jeol Ltd., Tokyo, Japan) at IGM. Grains previously analyzed using EDS were selected for this purpose. The operating conditions were as follows: beam diameter of 1–2 μm, accelerating voltage of 20 kV, beam current of 30 nA, and counting time of 10 (5 + 5) s for each element. The following standards were used for opaque and related minerals: $MgFe_2O_4$ (Fe and Mg), $MnFe_2O_4$ (Mn), $MgAl_2O_4$ (Al), $ZnFe_2O_4$ (Zn), rutile (Ti), $NiFe_2O_4$ (Ni), V_2O_5 (V), Cr_2O_3 (Cr), diopside (Ca and Si), albite (Na), orthoclase (K), and fluorapatite (P). Correction for matrix effects was done using a PAP routine [22]. The precision of analysis for major elements was better than 2% relative uncertainty. The detection limits for elements are (in ppm): Si—196; Ti—150; Cr—248; V—141; Al—255; Fe—146; Mn—122; Mg—168; Ca—105; Na—337; K—85; Zn—266; Cu—226; P—259.

Raman spectroscopy was used to characterize Cu-rich-magnesioferrite in the Tolbachik rock. We used a LabRAM HR 800 mm (HORIBA Scientific Ltd., Lat Krabang, Thailand) spectrometer equipped with a CCD detector and coupled to an Olympus BX40 (Tokyo, Japan) confocal microscope (objective ×100) at IGM. A semiconductor laser emitting at 514.5 nm with a nominal power output of 50 mW was used for excitation. In each case, 20 spectra were recorded for 20 s each at a hole diameter of 100 μm and integrated. The spectra were recorded between 100 and 1200 cm^{-1}, and the monochromator was calibrated using the 520.7 cm^{-1} Raman line of elemental Si.

All data are summarized in Tables 1–4 and Figures 4–11, and also in Supplementary Data (Tables S1–S6, Figures S1 and S2).

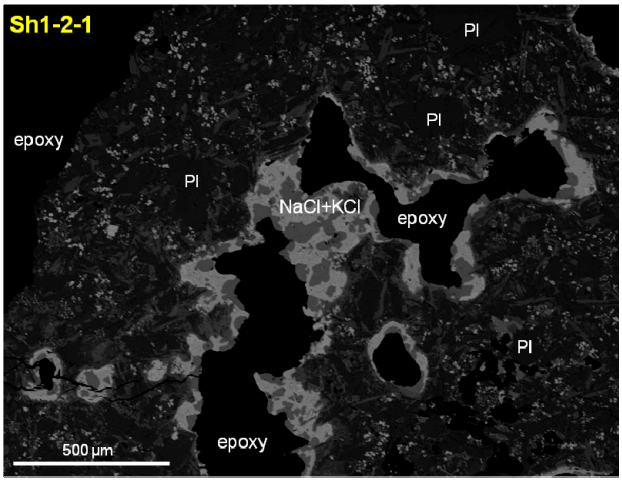

Figure 4. BSE image of a fragment of host rock with chloride covering on the wall and vesicles, Duplex lava tube.

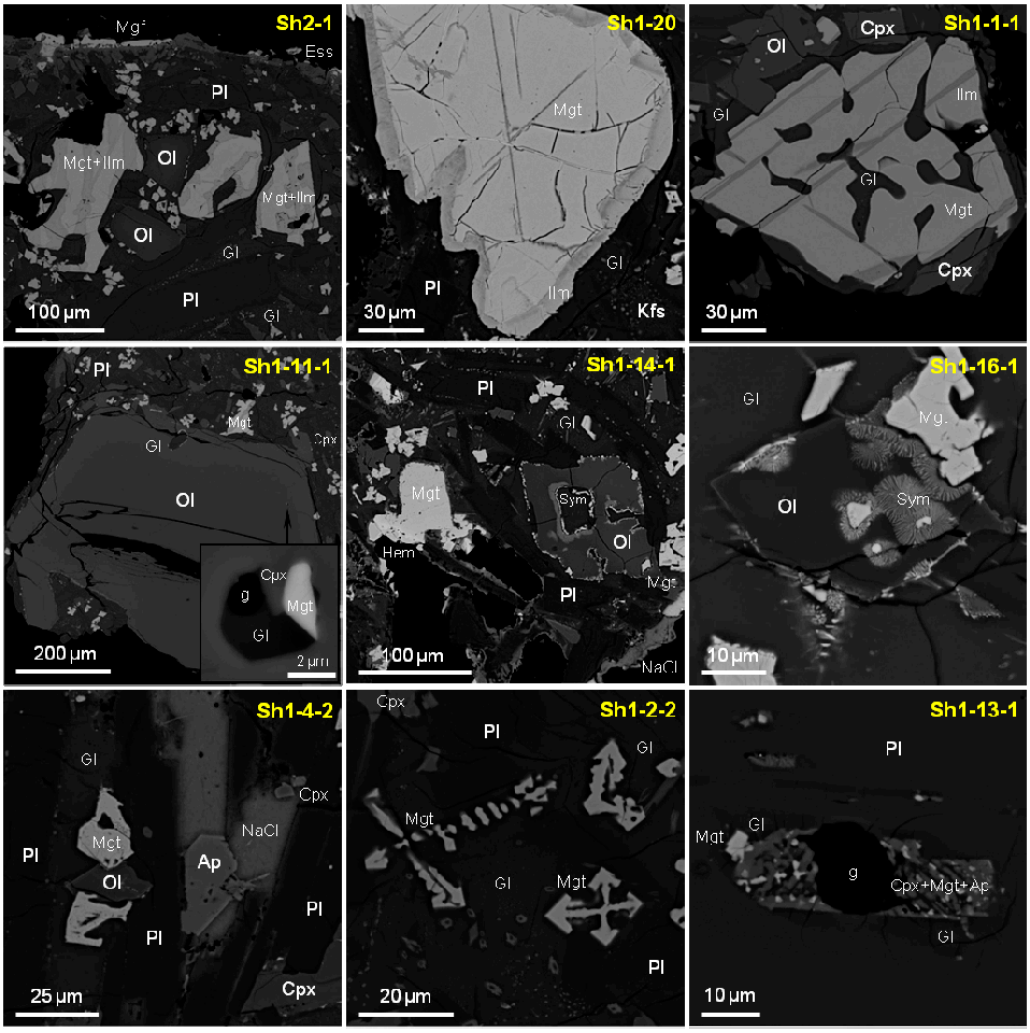

Figure 5. BSE images of mineral associations in the host rock, Duplex lava tube. Gl—silica-rich glass, sometimes with globules of former Si-poor Ca-Fe-P-rich glass; Pl—plagioclase; Kfs—K-feldspar; Mgt—Ti-rich magnetite; Ilm—ilmenite; Cpx—subcalcium diopside; Ol—olivine; Ap—fluorapatite; Mgf—Cu-rich magnesioferrite; Hem—hematite; Ess—esseneite; Sym—reactionary rim on olivine; g—gas bubble in silicate-melt inclusions.

4. Mineral Assemblages in Vesicular Trachyandesite

As mentioned above, chloride-sulfate mineralization is present at the surface as colorful incrustations around incandescent gas-venting skylights and cracks in the lava tubes [12–15]. In contrast, the interior of the recently-cooled parts of lava tubes, especially around wall fractures and stalactites, is coated by a fine-grained, grayish-white material. The studied mineral assemblage, covering the vesicular trachyandesite in the Duplex tube (Figures 3 and 4), is sulfate-free and consists of intergrowths of Na-K-chlorides, tenorite (CuO), magnesioferrite, hematite and newly-formed Ca-Fe-rich silicates [2]. Three individual zones may be conventionally subdivided: (i) host trachyandesite, (ii) reactionary zone, and (iii) chloride crust.

4.1. Host Trachyandesite Rock

According to previous studies, all of the 2012–2013 Tolbachik lavas fall into the basaltic trachyandesite field, with some of them close to shoshonitic in composition [23]. The studied trachyandesite sample is highly vesicular, where the sizes of some vesicles are up 1 cm. In general, plagioclase ($An_{37–70}$), olivine ($Fo_{71–79}$, rarely up to Fo_{87}), subcalcium diopside ($En_{33–42}Fs_{15–20}Wo_{40–48}$), and Ti–Cr-rich magnetite (up to 5 wt % Cr_2O_3) occur as phenocrysts and microphenocrysts (Figures 4 and 5). Sometimes magnesioferrite occurs as thin rims on magnetite phenocrysts. The groundmass in this naturally solidified sample is sometimes finely crystallized with dendritic crystals, which consists of clinopyroxene (augite), Ti-rich magnetite (up to 15 wt % TiO_2, or decay of magnetite + ilmenite/ulvöspinel), fluorapatite, K-feldspar ($Or_{74–90}$), and locally Si-rich glass (SiO_2—65–71 wt %).

Furthermore, this glass commonly contains globules of former Fe–Ca–Ti–P-rich and Si-poor glass (up to 10 μm, now occurring as fine-grained aggregate of pyroxene + fluorapatite + magnetite), indicating that silicate–silicate liquid immiscibility and rapid quenching in the late stages of crystallization (Figure 6). It should be noted that silicate–silicate liquid immiscibility was also observed in secondary melt inclusions in plagioclase, whereas melt inclusions in olivine and Ti-magnetite are primary in origin and consist of glass or glass + clinopyroxene + magnetite + shrinkage bubble (Figure 5). The chemical compositions of the main rock-forming minerals from the Tolbachik 2012–2013 eruption are presented in References [23,24]. Chemical data (analyses and elemental maps) for minerals and glasses for the studied trachyandesite sample are presented in Supplementary (Tables S1–S5, Figure S1).

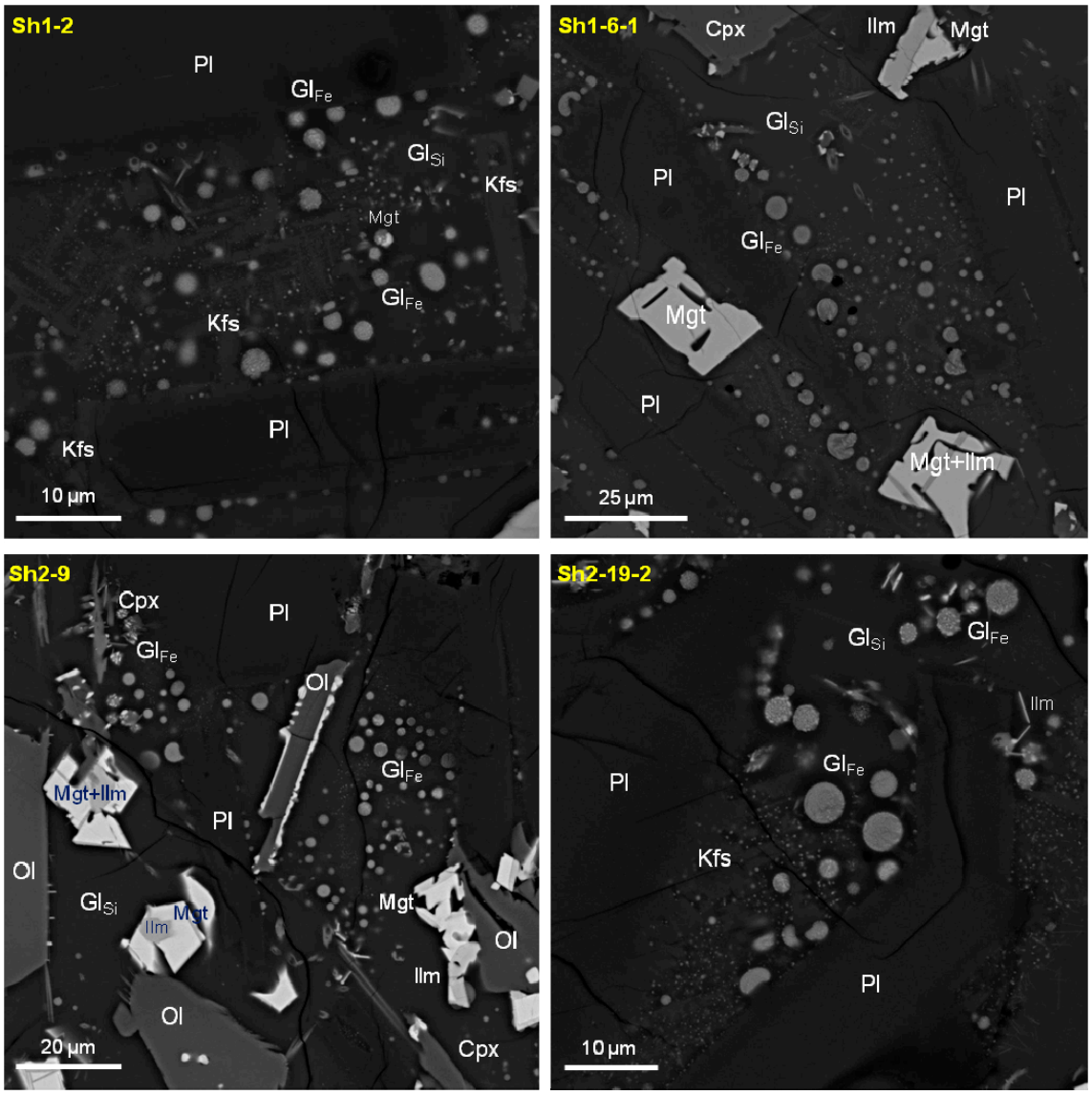

Figure 6. BSE images of interstitial silicate-silicate liquid immiscibility in the host rock, Duplex lava tube. Gl_{Si}—silica-rich glass; Gl_{Fe}—globules of former Si-poor Ca–Fe–P-rich glass; Pl—plagioclase; Kfs—K-feldspar; Mgt—Ti-rich magnetite; Ilm—ilmenite or ulvöspinel (in solid decay); Cpx—subcalcium diopside; Ol—olivine.

4.2. Reactionary Zone

The studied rock contains abundant coatings of chlorides + tenorite. This may be related to local gas streams penetrating the host rock. Nevertheless, vesicles situated 1 cm away from the main gas inflow contain significantly less chlorides and tenorite, or are essentially free of them. The thickness of the reactionary zone may be up to 100 µm and is represented by high-Ca silicates, hematite, and Cu-bearing magnesioferrite, and rarely tenorite (Figures 7 and 8). It sometimes has a deep yellow color due to the abundance of Ca-silicates. In general, we identified two subdivisions: Ca-rich silicates and Fe–Cu-oxides.

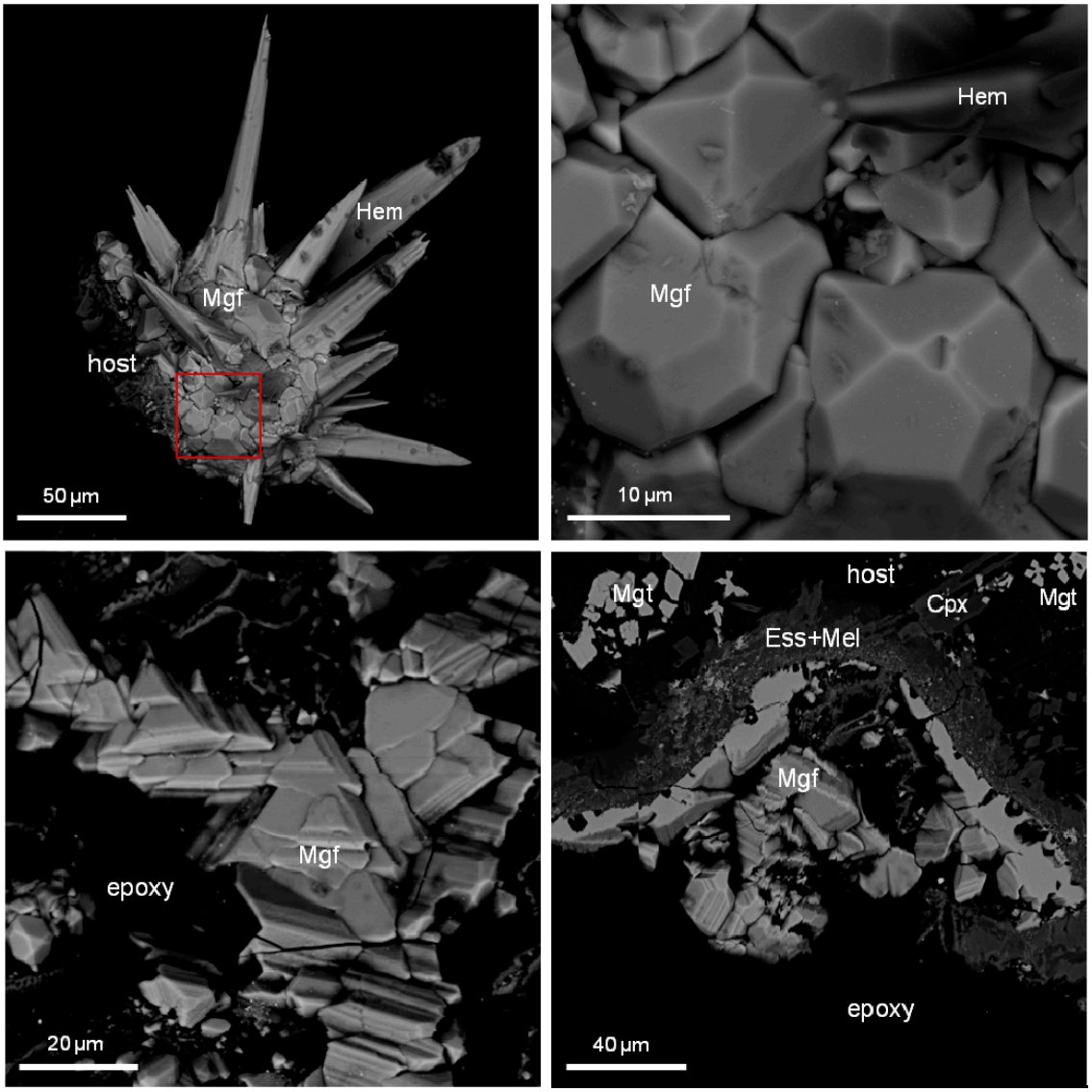

Figure 7. BSE images of cube-octahedral and octahedral crystals of Cu-rich magnesioferrite in vesicles of the host rock, Duplex lava tube. Mgf—Cu-rich magnesiferrite; Hem—hematite; host—host vesicular trachybasalt; Mgt—magnetite; Cpx—subcalcium diopside; Ess + Mel—esseneite + melilite.

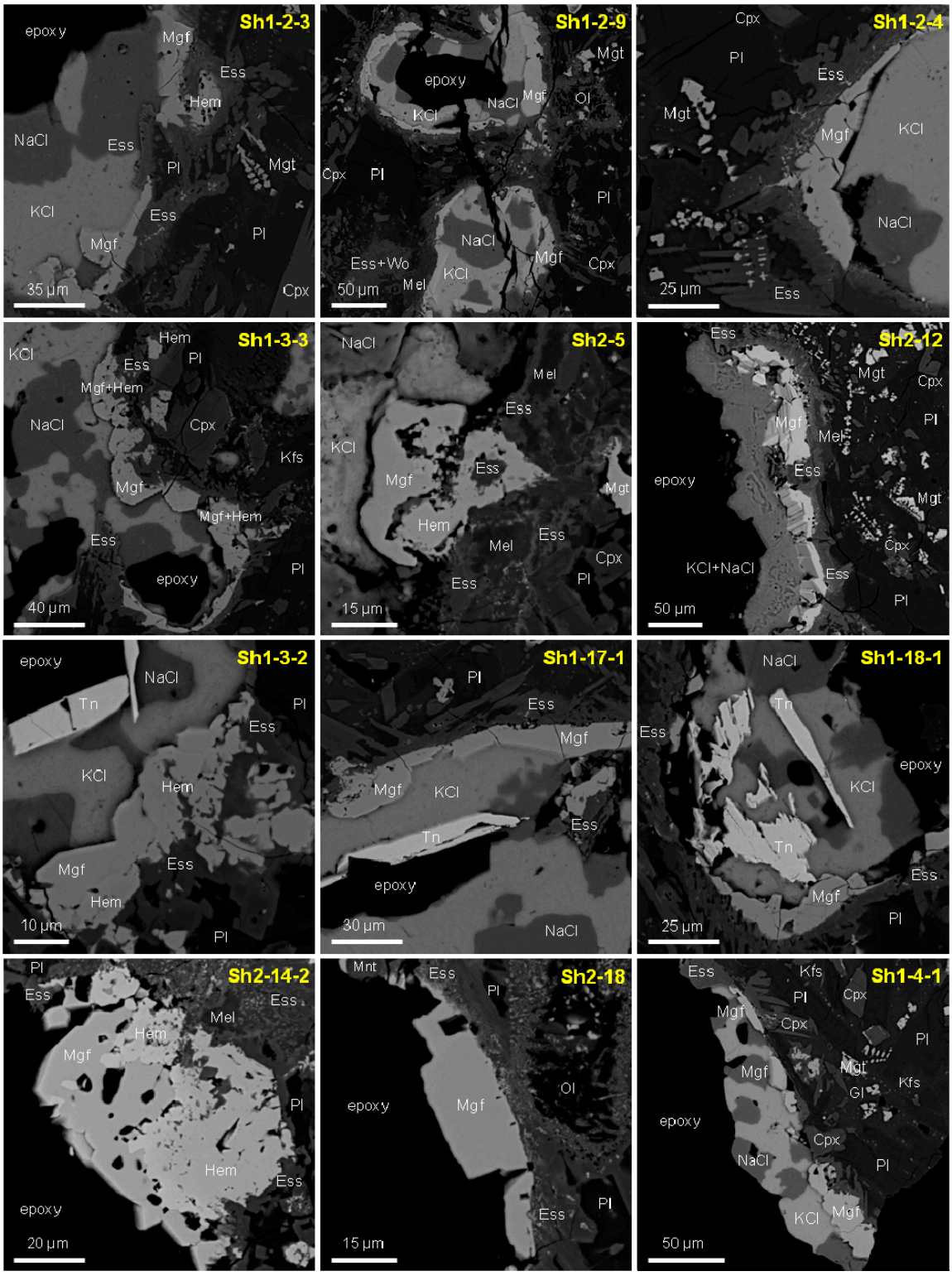

Figure 8. BSE images showing the associations with Cu-rich magnesioferrite in vesicles of the host rock, Duplex lava tube. Mgf—Cu-rich magnesiferrite; Hem—hematite; Tn—tenorite; Ess—esseneite; Mel—Na-rich melilite; Mnt—monticellite; Cpx—subcalcium diopside; Mgt—Ti-rich magnetite; Pl—plagioclase; Kfs—K-feldspar; Ol—olivine; Gl—silica-rich glass, sometimes with globules of former Si-poor Ca–Fe–P-rich glass.

Table 1. Chemical composition (EMPA-WDS, wt %) of clinopyroxene and melilite from reactionary zone around vesicles, Duplex lava tube.

Sample	Clinopyroxene										Melilite						
	Sh1-2-5		Sh1-2-9	Sh1-3-1	Sh1-3-1	Sh2-8	Sh2-11	Sh2-14	Sh2-14-2	*n* = 8	Sh1-2-9		Sh2-5	Sh2-8	Sh2-12	Sh2-14-2	*n* = 6
	c	*r*	*c*	*c*	*c*	*c*	*c*	*c*	*c*		*c*	*r*	*c*	*c*	*c*	*c*	
SiO_2	30.93	31.27	34.85	33.73	34.22	33.26	33.40	34.09	33.60	33.22	37.53	37.97	37.10	37.78	38.61	38.13	37.85
TiO_2	0.95	0.99	0.86	1.77	1.31	1.32	1.46	0.50	0.43	1.14	0.07	0.06	0.07	0.07	0.06	0.11	0.07
Cr_2O_3	0.05	0.00	0.00	0.00	0.00	0.00	0.03	0.00	0.00	0.01	0.00	0.00	0.00	0.00	0.00	0.00	0.00
Al_2O_3	24.52	23.73	20.02	17.81	17.57	17.62	17.87	20.24	17.04	19.92	24.22	23.48	24.49	23.06	19.73	19.69	22.45
Fe_2O_3	15.96	15.47	13.34	16.37	16.44	19.06	17.64	15.92	20.62	16.27	0.81	0.03	0.14	2.42	2.28	3.27	1.49
FeO	0.38	1.15	1.41	1.35	1.57	0.71	0.51	0.01	0.04	0.89	0.78	1.44	1.64	0.00	0.04	0.12	0.67
MnO	0.41	0.41	0.39	0.43	0.47	0.50	0.39	0.35	0.40	0.42	0.10	0.04	0.03	0.19	0.11	0.05	0.09
CuO	0.11	0.11	0.00	0.13	0.18	0.00	0.00	0.00	0.00	0.07	0.00	0.00	0.00	0.00	0.00	0.09	0.01
MgO	3.11	3.12	5.13	4.97	4.84	4.63	5.09	5.09	4.99	4.50	0.17	0.46	0.78	0.65	2.60	2.82	1.25
CaO	23.97	24.04	24.10	23.70	23.70	23.53	23.61	23.86	23.72	23.81	29.50	29.68	29.01	29.11	29.38	29.48	29.36
Na_2O	0.15	0.08	0.16	0.23	0.21	0.29	0.22	0.26	0.18	0.20	7.05	6.87	6.63	7.20	6.53	6.33	6.77
K_2O	0.00	0.00	0.00	0.00	0.00	0.00	0.00	0.00	0.00	0.00	0.11	0.09	0.15	0.10	0.10	0.05	0.10
P_2O_5	0.00	0.06	0.05	0.13	0.04	0.00	0.00	0.00	0.00	0.04	0.00	0.00	0.00	0.00	0.00	0.00	0.00
Sum	100.53	100.44	100.29	100.61	100.55	100.92	100.22	100.32	101.03	100.48	100.33	100.12	100.02	100.58	99.44	100.13	100.10
Formula	based on four cations and six oxygens										based on five cations and seven oxygens						
Si	1.190	1.207	1.335	1.306	1.327	1.291	1.298	1.308	1.304	1.283	1.658	1.682	1.645	1.668	1.725	1.699	1.679
Al	0.810	0.791	0.664	0.690	0.672	0.709	0.702	0.692	0.696	0.716	0.342	0.318	0.355	0.332	0.275	0.301	0.321
P	0.000	0.002	0.002	0.004	0.001	0.000	0.000	0.000	0.000	0.001	0.000	0.000	0.000	0.000	0.000	0.000	0.000
Sum T	2.000	2.000	2.000	2.000	2.000	2.000	2.000	2.000	2.000	2.000	2.000	2.000	2.000	2.000	2.000	2.000	2.000
Ti	0.027	0.029	0.025	0.051	0.038	0.039	0.043	0.014	0.013	0.033	0.002	0.002	0.002	0.002	0.002	0.004	0.002
Cr	0.002	0.000	0.000	0.000	0.000	0.000	0.001	0.000	0.000	0.000	0.000	0.000	0.000	0.000	0.000	0.000	0.000
Al	0.302	0.288	0.240	0.123	0.131	0.097	0.117	0.223	0.083	0.190	0.920	0.908	0.924	0.868	0.764	0.733	0.853
Fe^{3+}	0.462	0.449	0.384	0.477	0.480	0.557	0.516	0.459	0.602	0.473	0.027	0.001	0.005	0.081	0.077	0.110	0.050
Fe^{2+}	0.012	0.037	0.045	0.044	0.051	0.023	0.017	0.000	0.001	0.029	0.029	0.053	0.061	0.000	0.001	0.004	0.025
Mn	0.013	0.013	0.013	0.014	0.015	0.016	0.013	0.012	0.013	0.014	0.004	0.002	0.001	0.007	0.004	0.002	0.003
Cu	0.003	0.003	0.000	0.004	0.005	0.000	0.000	0.000	0.000	0.002	0.000	0.000	0.000	0.000	0.000	0.003	0.000
Mg	0.178	0.180	0.293	0.287	0.280	0.268	0.295	0.291	0.289	0.259	0.011	0.030	0.051	0.043	0.173	0.187	0.082
Sum O	1.000	1.000	1.000	1.000	1.000	1.000	1.000	1.000	1.001	1.000	0.992	0.996	1.044	1.001	1.021	1.043	1.016
Ca	0.988	0.994	0.989	0.983	0.984	0.979	0.983	0.981	0.986	0.985	1.397	1.409	1.378	1.377	1.406	1.407	1.396
Na	0.011	0.006	0.012	0.017	0.016	0.022	0.017	0.019	0.013	0.015	0.604	0.590	0.570	0.616	0.566	0.547	0.582
K	0.000	0.000	0.000	0.000	0.000	0.000	0.000	0.000	0.000	0.000	0.006	0.005	0.008	0.005	0.005	0.003	0.005
Sum P	1.000	1.000	1.000	1.000	1.000	1.000	1.000	1.000	0.999	1.000	2.007	2.004	1.956	1.999	1.977	1.957	1.983

FeO and Fe_2O_3 were calculated via charge balance; *c*, *r*—core and rim of grains. The sample numbers in this and further tables indicate the numbers of BSE images in Figures Figures 4–6, 8, S1 and S2.

Table 2. Chemical composition (EMPA-WDS, wt %) of hematite from vesicles, Duplex lava tube.

Sample	Sh1-4	Sh1-2-5	Sh1-3-2		Sh1-3-2-2	Sh1-3-3		Sh1-3-3	Sh1-20-2	Sh2-3	Sh2-3	Sh2-4	Sh2-5	Sh2-14-2					Sh2-16	Sh2-17
	c	*c*	*c*	*r*	*c*	*c*	*r*	*c*	*c*	*c*	*c*	*c*	*c*	*c*	*m*	*r*	*r*	*r*	*c*	*c*
TiO_2	12.83	11.22	10.32	7.36	7.02	7.86	7.03	6.14	3.24	1.28	0.87	5.77	2.84	12.10	10.86	4.20	3.21	1.97	2.03	10.09
Cr_2O_3	0.07	0.49	0.05	0.00	0.00	0.01	0.00	0.04	0.00	0.00	0.02	0.00	0.00	0.71	0.31	0.00	0.00	0.05	0.00	0.00
V_2O_3	0.13	0.04	0.02	0.05	0.00	0.03	0.00	0.02	0.00	0.00	0.03	0.00	0.00	0.00	0.00	0.00	0.00	0.00	0.08	0.00
Al_2O_3	2.81	1.42	0.85	0.74	0.88	1.28	1.06	0.48	0.64	0.27	0.41	0.64	0.66	1.43	1.21	1.65	0.49	1.05	0.51	0.51
Fe_2O_3	73.87	81.09	82.19	87.08	87.19	85.96	87.67	88.58	94.26	97.62	97.87	89.88	94.34	78.53	81.52	91.56	94.28	95.73	96.42	83.36
FeO	3.34	0.10	0.06	0.02	0.10	0.05	0.15	0.13	0.02	0.09	0.01	0.08	0.05	1.73	0.97	0.03	0.00	0.05	0.03	0.08
MnO	0.93	0.43	1.43	0.72	0.74	0.63	0.63	1.11	0.22	0.09	0.14	0.41	0.35	0.52	0.54	0.41	0.39	0.30	0.17	0.85
MgO	2.69	4.60	3.69	2.44	2.31	3.17	2.58	1.34	1.21	0.31	0.11	2.24	0.68	4.57	4.37	1.67	1.03	0.49	0.80	4.10
CaO	0.20	0.23	0.39	0.23	0.26	0.20	0.15	0.45	0.39	0.21	0.16	0.45	0.31	0.24	0.16	0.15	0.31	0.35	0.11	0.16
ZnO	0.17	0.08	0.08	0.04	0.06	0.04	0.05	0.06	0.00	0.00	0.03	0.00	0.00	0.06	0.06	0.05	0.06	0.00	0.00	0.00
CuO	2.29	1.10	0.69	1.32	1.05	0.50	0.78	1.39	0.03	0.17	0.22	0.14	0.59	0.14	0.22	0.14	0.23	0.11	0.06	0.68
Sum	99.31	100.79	99.77	100.00	99.63	99.73	100.09	99.72	100.01	100.04	99.87	99.61	99.82	100.04	100.21	99.85	99.99	100.10	100.21	99.83
Formula	based on two cations and three oxygens																			
Ti	0.246	0.211	0.198	0.143	0.137	0.151	0.136	0.121	0.064	0.025	0.017	0.113	0.056	0.229	0.206	0.082	0.063	0.039	0.040	0.193
Cr	0.001	0.010	0.001	0.000	0.000	0.000	0.000	0.001	0.000	0.000	0.000	0.000	0.000	0.014	0.006	0.000	0.000	0.001	0.000	0.000
V	0.003	0.001	0.000	0.001	0.000	0.001	0.000	0.000	0.000	0.000	0.001	0.000	0.000	0.000	0.000	0.000	0.000	0.000	0.002	0.000
Al	0.084	0.042	0.025	0.023	0.027	0.039	0.032	0.015	0.020	0.008	0.013	0.020	0.020	0.042	0.036	0.050	0.015	0.032	0.016	0.015
Fe^{3+}	1.419	1.526	1.577	1.691	1.700	1.657	1.696	1.743	1.853	1.941	1.952	1.755	1.867	1.486	1.546	1.786	1.858	1.889	1.903	1.598
Fe^{2+}	0.071	0.002	0.001	0.000	0.002	0.001	0.003	0.003	0.000	0.002	0.000	0.002	0.001	0.036	0.020	0.001	0.000	0.001	0.001	0.002
Mn	0.020	0.009	0.031	0.016	0.016	0.014	0.014	0.024	0.005	0.002	0.003	0.009	0.008	0.011	0.011	0.009	0.009	0.007	0.004	0.018
Mg	0.102	0.172	0.140	0.094	0.089	0.121	0.099	0.052	0.047	0.012	0.004	0.087	0.027	0.171	0.164	0.064	0.040	0.019	0.031	0.156
Ca	0.005	0.006	0.011	0.006	0.007	0.005	0.004	0.013	0.011	0.006	0.005	0.012	0.009	0.006	0.004	0.004	0.009	0.010	0.003	0.004
Zn	0.003	0.001	0.002	0.001	0.001	0.001	0.001	0.001	0.000	0.000	0.001	0.000	0.000	0.001	0.001	0.001	0.001	0.000	0.000	0.000
Cu	0.044	0.021	0.013	0.026	0.021	0.010	0.015	0.027	0.001	0.003	0.004	0.003	0.012	0.003	0.004	0.003	0.005	0.002	0.001	0.013

FeO and Fe_2O_3 were calculated via charge balance; *c*, *r*—core and rim of grains.

4.2.1. Silicates

The interior of the trachyandesite subzone consists of esseneite, Na-melilite (alumoåkermanite), wollastonite, monticellite, and titanite, as well as grossular garnet and Cl-SO_4-rich fluorapatite. These minerals form fine-grained intergrowths, which replace trachyandesite silicates, mainly clinopyroxene and plagioclase (Figures 7 and 8). Dominant esseneite and melilite are visible in transmitted light due to their yellow color. The average formulae for these minerals are $(Ca_{0.98}Na_{0.02})(Fe^{3+}{}_{0.48}Mg_{0.26}Al_{0.19}Fe^{2+}{}_{0.03}Ti_{0.03}Mn_{0.01})(Si_{1.28}Al_{0.72})O_6$ and $(Ca_{1.40}Na_{0.59}K_{0.01})(Al_{0.85}Mg_{0.08}Fe_{0.07})(Si_{1.68}Al_{0.32})O_7$, respectively (Table 1). Due to the small sizes of other minerals, their compositions were only characterized using SEM-EDS (Figure 8, Figures S1 and S2).

4.2.2. Fe–Cu-Oxides

These oxides occur mainly on vesicle walls and form ideal crystal shapes (Figure 7). The relationships of Fe–Cu-oxides suggest the following sequence of crystallization: Ti-rich hematite ± Cu-free magnesioferrite → Cu-bearing hematite → Cu-rich magnesioferrite → tenorite (indicates decreasing Fe and increasing of Cu; Figure 8 and S2). Our observations show that hematite Fe_2O_3 (confirmed by Raman spectra) and magnesioferrite $MgFe_2O_4$ can form both as a replacement of magmatic oxides in the trachyandesite (magnetite and ilmenite) and by direct crystallization on the vesicular walls. Cu-rich magnesioferrite forms overgrowths around hematite using it as seal, or crystallizing directly on the vesicular walls. Similar relationships between hematite and Cu-rich spinel-group minerals were also described for the Arsenatnaya fumarole [5].

In general, cores of hematite grains may contain inclusions of Cu-free magnesioferrite and unidentified Ca–Ti-phases (titanite or perovskite), rarely Ca-silicates. In contrast, Cu-rich magnesioferrite hosts inclusions of hematite and sometimes Ca-silicates. No sulfates or chlorides were found in minerals from this reactionary subzone. Chemical zonation is common in hematite, where it is represented by a Ti–Mg–Al-rich core (TiO_2—up to 13 wt %; MgO—up to 4.6 wt %; Al_2O_3—up to 2.8 wt %) and rim, which is poor in these elements (Figure S2A–E). The concentration of CuO in hematite may be up 2.3 wt %. Cu-rich magnesioferrite and tenorite do not show drastic variations in composition. Tenorite contains FeO up to 1.0 wt %. Chemical data for hematite and tenorite are presented in Tables 2 and 3. The composition of magnesioferrite is shown below (Section 5).

Table 3. Composition (EMPA-WDS, wt %) of tenorite from Duplex lava tube, Tolbachik.

Sample	CuO	FeO	Sum
Sh1-3-1	99.86	0.03	99.89
Sh1-3-2	99.14	0.71	99.85
Sh1-17-1	98.74	0.98	99.72
Sh1-18-1	99.26	0.49	99.75
Sh1-20-2	99.10	0.89	99.99

Individual crystals from chloride-rich vesicles were analyzed.

Table 4. Representative compositions (EMPA-WDS, wt %) of Cu-containing magnesioferrite from vesicles in trachyandesite, Duplex lava tube, Tolbachik.

Sample		TiO_2	Al_2O_3	Fe_2O_3	FeO	MnO	MgO	CaO	ZnO	CuO	Sum	Ti	Al	Fe^{3+}	$\sum R^{3+}$	Fe^{2+}	Mn	Mg	Ca	Zn	Cu	$\sum R^{2+}$
		wt %										Formula based on three cations and four oxygens										
Sh2-3	***inc***	0.94	1.99	73.56	6.25	0.70	15.94	0.35	0.18	0.22	100.13	0.024	0.079	1.873	1.976	0.177	0.020	0.804	0.013	0.005	0.006	1.024
Sh1-1-6	***inc***	1.73	3.24	71.94	0.56	2.52	18.51	0.06	0.62	1.15	100.32	0.043	0.126	1.788	1.957	0.015	0.070	0.911	0.002	0.015	0.029	1.043
Sh2-17	***c***	0.78	1.00	74.03	0.06	2.71	15.06	0.15	0.35	5.82	99.96	0.020	0.041	1.919	1.980	0.002	0.079	0.773	0.006	0.009	0.151	1.020
Sh2-11	***c***	0.68	1.82	73.04	0.08	2.11	15.02	0.40	0.11	6.46	99.86	0.018	0.074	1.887	1.982	0.002	0.061	0.769	0.015	0.003	0.168	1.018
	r	0.67	1.81	72.79	0.08	2.22	14.10	0.62	0.10	7.62	100.00	0.017	0.074	1.892	1.983	0.002	0.065	0.726	0.023	0.003	0.199	1.017
Sh2-18	***c***	0.39	0.84	74.29	0.44	1.84	14.20	0.25	0.10	7.42	99.77	0.010	0.035	1.945	1.990	0.013	0.054	0.736	0.009	0.002	0.195	1.010
Sh2-14-2	***c***	0.39	1.34	73.01	0.89	2.31	12.80	0.27	0.14	8.83	99.98	0.010	0.055	1.924	1.990	0.026	0.068	0.668	0.010	0.004	0.234	1.010
	m	0.33	1.55	72.73	0.96	2.33	12.69	0.22	0.19	8.88	99.88	0.009	0.064	1.919	1.991	0.028	0.069	0.663	0.008	0.005	0.235	1.009
	r	0.39	1.58	72.61	0.71	2.38	12.97	0.27	0.12	8.64	99.70	0.010	0.065	1.913	1.990	0.021	0.070	0.677	0.010	0.003	0.229	1.010
	r	0.34	1.31	72.86	0.48	2.32	12.80	0.24	0.19	9.06	99.60	0.009	0.054	1.928	1.991	0.014	0.069	0.671	0.009	0.005	0.241	1.009
Sh2-16	***c***	0.12	1.03	74.09	0.00	2.09	13.45	0.28	0.11	8.55	99.73	0.003	0.042	1.951	1.997	0.000	0.062	0.702	0.011	0.003	0.226	1.003
	r	0.11	1.00	73.87	0.29	2.00	13.06	0.19	0.14	9.04	99.70	0.003	0.041	1.953	1.997	0.009	0.060	0.684	0.007	0.004	0.240	1.003
Sh2-10	***c***	0.23	2.43	72.37	0.01	2.20	13.50	0.19	0.11	8.92	99.96	0.006	0.099	1.889	1.994	0.000	0.065	0.698	0.007	0.003	0.234	1.006
	r	0.22	2.35	71.85	0.04	2.18	13.12	0.23	0.08	9.29	99.36	0.006	0.097	1.891	1.994	0.001	0.064	0.684	0.009	0.002	0.245	1.006
Sh1-2-9	***c***	0.24	1.79	72.61	0.00	2.17	12.72	0.28	0.26	9.84	99.92	0.006	0.074	1.914	1.994	0.000	0.064	0.664	0.011	0.007	0.260	1.006
Sh1-2-8	***c***	0.31	2.18	71.89	0.00	2.15	12.51	0.42	0.28	10.16	99.89	0.008	0.090	1.894	1.992	0.000	0.064	0.653	0.016	0.007	0.269	1.008
	r	0.26	2.01	72.22	0.03	2.21	12.48	0.38	0.31	10.09	99.99	0.007	0.083	1.903	1.993	0.001	0.066	0.652	0.014	0.008	0.267	1.007
Sh2-12	***c***	0.24	1.32	72.94	0.09	2.10	12.34	0.44	0.10	10.31	99.88	0.006	0.055	1.933	1.994	0.003	0.063	0.648	0.016	0.003	0.274	1.006
Sh1-2-4	***c***	0.20	1.84	72.39	0.00	2.15	12.04	0.41	0.25	10.89	100.17	0.005	0.076	1.913	1.995	0.000	0.064	0.630	0.015	0.007	0.289	1.005
Sh1-2-7	***c***	0.21	1.78	71.96	0.07	2.12	11.35	0.39	0.40	11.85	100.12	0.006	0.074	1.915	1.994	0.002	0.064	0.598	0.015	0.010	0.317	1.006
	r	0.22	1.87	71.69	0.00	2.06	11.35	0.43	0.47	11.83	99.92	0.006	0.078	1.910	1.994	0.000	0.062	0.599	0.016	0.012	0.316	1.006
	r	0.24	1.76	71.94	0.04	2.08	11.44	0.46	0.44	11.64	100.04	0.006	0.073	1.914	1.994	0.001	0.062	0.603	0.017	0.012	0.311	1.006
	r	0.25	1.82	71.09	0.00	1.96	10.67	0.39	0.42	13.09	99.69	0.007	0.076	1.910	1.993	0.000	0.059	0.568	0.015	0.011	0.353	1.007
Sh1-2-3	***c***	0.21	2.06	71.46	0.05	2.11	11.24	0.46	0.38	11.99	99.96	0.006	0.086	1.903	1.994	0.001	0.063	0.593	0.017	0.010	0.321	1.006
Sh2-5	***c***	0.29	1.07	71.62	0.82	1.92	10.36	0.19	0.75	12.56	99.58	0.008	0.045	1.939	1.992	0.025	0.059	0.556	0.007	0.020	0.341	1.008
Sh1-17-1	***c***	0.36	0.99	71.61	0.00	2.24	10.05	0.40	0.80	13.47	99.92	0.010	0.042	1.938	1.990	0.000	0.068	0.539	0.015	0.021	0.366	1.010
Sh1-3-2-2	***c***	0.43	1.54	70.75	0.00	2.60	9.90	0.16	0.73	13.91	100.02	0.012	0.065	1.912	1.988	0.000	0.079	0.530	0.006	0.019	0.377	1.012
Sh1-18-1	***c***	0.46	1.13	70.93	0.02	2.26	9.61	0.14	0.74	14.68	99.98	0.013	0.048	1.927	1.987	0.001	0.069	0.517	0.006	0.020	0.400	1.013
Sh1-3-2	***c***	0.54	1.02	70.77	0.00	2.58	9.39	0.17	0.68	14.79	99.95	0.015	0.043	1.927	1.985	0.000	0.079	0.507	0.007	0.018	0.404	1.015
Sh1-3-1	***c***	0.47	1.01	70.35	0.05	2.88	8.56	0.36	0.74	15.34	99.76	0.013	0.043	1.931	1.987	0.002	0.089	0.465	0.014	0.020	0.423	1.013
Sh1-3-1	***c***	0.54	0.79	69.83	0.03	2.77	7.47	0.40	0.79	17.27	99.90	0.015	0.034	1.935	1.985	0.001	0.086	0.410	0.016	0.021	0.480	1.015

FeO and Fe_2O_3 are calculated by charge balance; *c*, *m*, *r*—core, middle and rim of grains; *inc*—inclusion in hematite. All databases of EMPA-WDS analyses for Cu-rich magnesioferrite see Supplementary Table S6.

4.3. Chloride Crust

Halite and sylvite occur in approximately equal proportions and are the dominant chlorides on the rock surfaces and within the vesicles (Figures 3 and 4). Platy tenorite is scattered among the chloride masses and crystals commonly grow within open spaces. Small octahedral crystals (<3 μm) of native gold sometimes occur in association with Na–K, K–Cu, and Cu chlorides. Furthermore, oxychlorides may present among salt [2].

5. Morphology and Chemistry of Cu-Rich Magnesioferrite

Cu-rich magnesioferrite forms cube-octahedral or octahedral crystals (30–40 μm in size) in vesicle walls (Figure 7), as well as rarely occurring as inclusion in hematite (Figure S2B,E). In general, individual crystals are homogeneous in composition and do not exhibit any visible zoning (Figure S2A–E). However, variations for all analyzed grains are essential (Figures 9 and 10). Representative compositions of magnesioferrite are shown in Table 4 and a complete list of EMPA-WDS analyses is given in Supplementary Table S6. Most of grains on vesicle walls are Cu-bearing magnesioferrite $(Mg,Cu)Fe^{3+}{}_2O_4$ with 5.8–17.3 wt % CuO and with minor TiO_2 (up to 0.9 wt %), Al_2O_3 (up to 2.4 wt %), MnO (up 3.0 wt %), ZnO (up to 0.8 wt %), CaO (up to 0.4 wt %), and minimal FeO (up to 1.0 wt %, calculated values). However, the hematite-hosted inclusions are poor in CuO (0.2–1.0 wt %) and have mineral formulae ranging from $(Mg_{0.80}Fe^{2+}{}_{0.18}Mn_{0.02}Cu_{0.01}Zn_{0.01}Ca_{0.01})(Fe^{3+}{}_{1.87}Al_{0.09}Ti_{0.03})O_4$ to $(Mg_{0.91}Fe^{2+}{}_{0.02}Mn_{0.07}Cu_{0.03}Zn_{0.03})(Fe^{3+}{}_{1.79}Al_{0.13}Ti_{0.04})O_4$. Analyses by WDS and EDS data show that some grains of Cu-rich magnesioferrite exhibit weak zoning; the core-to-rim difference in the CuO content may reach 0.5–1.0 wt % (Table 4).

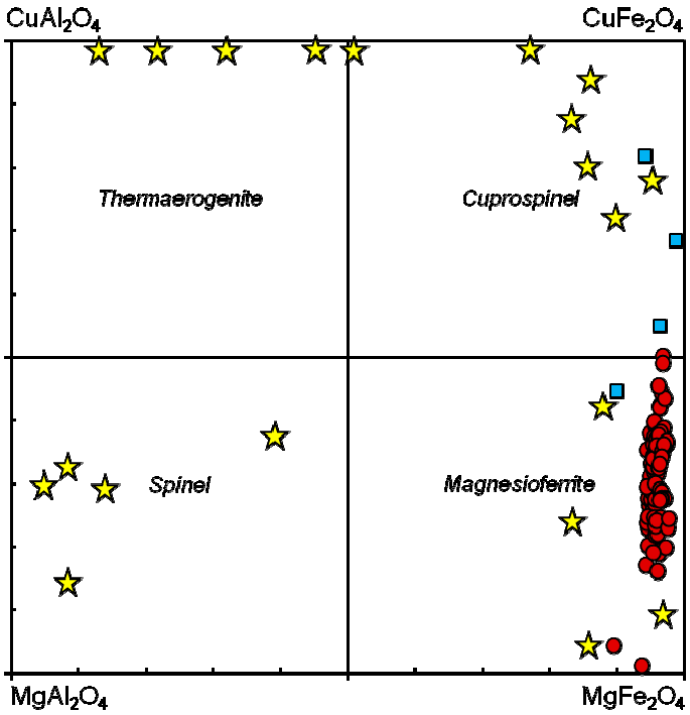

Figure 9. Classification diagram for the Mg–Cu–Al–Fe spinel-supergroup minerals. Circles—Cu–rich magnesioferrite from the Duplex lava tube, Tolbachik volcano, Kamchatka peninsula, Russia (our data, see database in Table S6); squares—cuprospinel (holotype) and Cu–rich magnesioferrite from burned dump of Consolidated Rambler mine, Newfoundland, Canada [1]; stars—thermaerogenite (holotype), Cu-rich spinel, Cu-rich magnesioferrite and cuprospinel from the Arsenatnaya fumarole, Second scoria cone of the 1975 Northern Breakthrough, Tolbachik volcano, Kamchatka peninsula, Russia [5]. Minor Zn in all analyses was added to Cu.

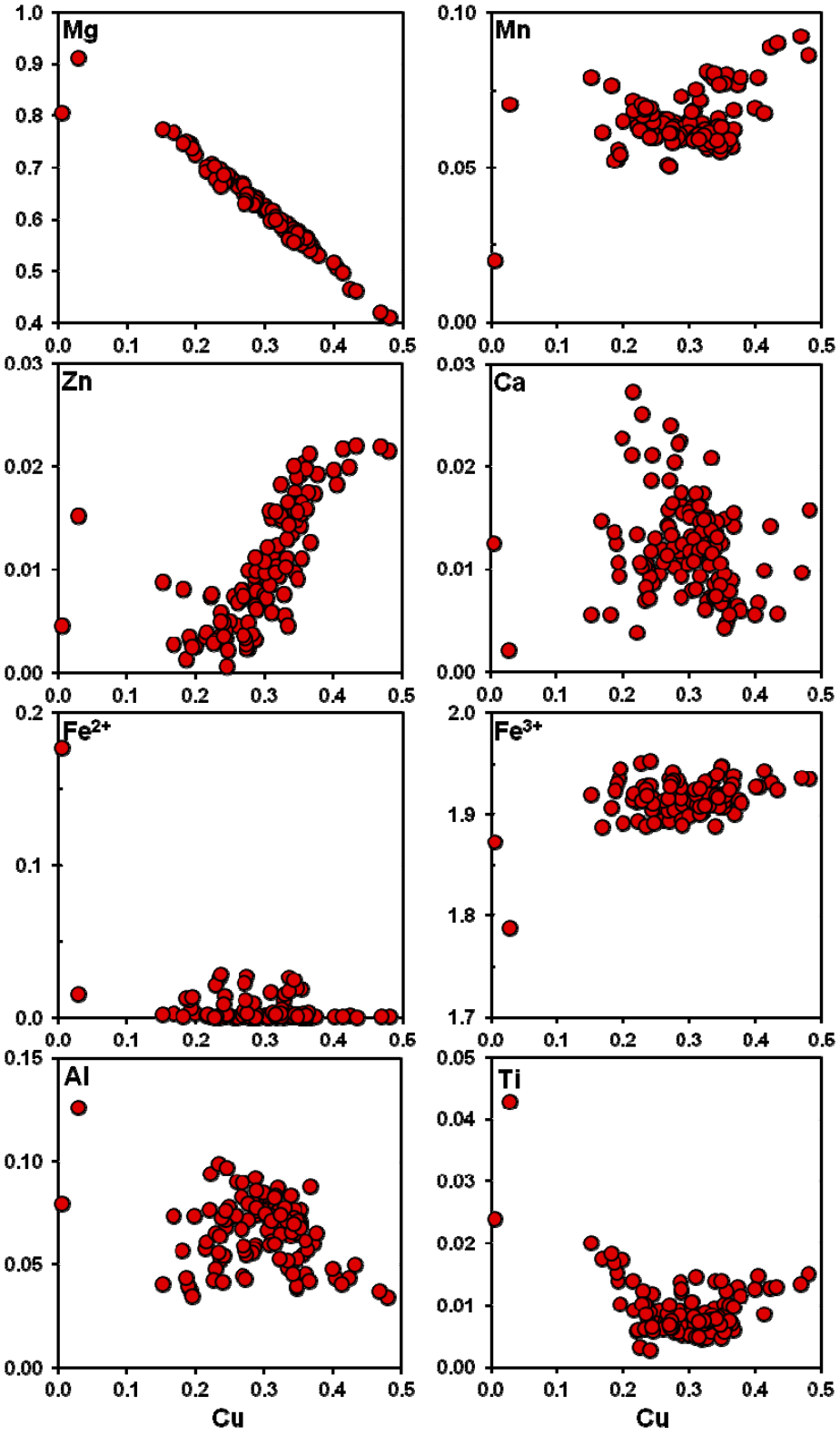

Figure 10. Variations of Cu vs. other elements (in *apfu*) for Cu-magnesioferrite from the Duplex lava tube, Tolbachik volcano, Kamchatka peninsula, Russia. Database of EMPA-WDS analyses (Table S6) were used.

In general, the classification diagram shows that all compositions fall into the magnesioferrite field (Figure 9) and content of the cuprospinel end-member mainly varies from 15–47 mol %. Only analyses with maximal CuO (17.3 wt %) are located on the 50% boundary between magnesoferrite and cuprospinel. Nominally such compositions should be classified as a Mg-rich cuprospinel: $(Cu_{0.48}Mg_{0.41}Mn_{0.09}Zn_{0.02}Ca_{0.02})(Fe^{3+}{}_{1.94}Al_{0.03}Ti_{0.02})O_4$. Furthermore, in contrast with chloride-filled vesicles, magnesioferrite from chloride-free vesicles (far from main gas flow) is poorer in CuO (6–9 wt %).

Bivariate plots showing Cu versus other elements for the Duplex Cu-magnesioferrite (Figure 10) demonstrate a pronounced negative correlation between Mg and Cu, strong positive Cu–Zn correlation and weak positive correlation for Cu and Mn. Other components do not show any dependence with Cu. This indicates that the isomorphic scheme $Mg^{2+} \leftrightarrow Cu^{2+}$ ($\pm Zn^{2+}$) is the main dependence for the Duplex magnesioferrite.

We were unable to obtain XRD and single-crystal data for the Duplex magnesioferrite due to its small sizes. Among synthetic ferrite spinels, only $CuFe_2O_4$ and $NiFe_2O_4$ compounds have both cubic and tetragonal modifications. Two polymorphs of $CuFe_2O_4$ may coexist together within nanocomposite material or ceramic of Cu-Fe-O [25–36]. The phase transition tetragonal $\leftrightarrow$ cubic $CuFe_2O_4$ is fixed at 402–440 °C [29,31]. However, the doping of any element in the $CuFe_2O_4$ structure inevitably transforms it into the cubic modification as a sole stable phase [30,36–38]. According to XRD and unit-cell data, all-natural Cu-rich spinels are cubic due to their complex composition [1,3–5]. We suggest that the Duplex Cu-containing magnesioferrite also has cubic symmetry.

6. Raman Spectroscopy for Cu-Rich Magnesioferrite

Eight Raman spectra were obtained for the Duplex magnesioferrite grains exhibiting different CuO contents. The best-fit spectra are presented in Figure 11. Our interpretation is based on new data for spinel-group minerals by D'Ippolito et al. [39]. In general, all presented spectra are very consistent in the band suite to that for ideal magnesioferrite: active modes at 208 ($F_{2g}1$), 330 (E_g1), 382 (E_g2), 479 ($F_{2g}2$), 560 ($F_{2g}3$), and 706 ($A_{1g}2$) cm^{-1}. The broad and strong band at ≈710 cm^{-1} (A_{1g} Raman mode) is the characteristic Raman feature of the end-member magnesioferrite and is related to the stretching mode of the Fe^{3+}-O in the tetrahedral site [39]. Other weaker Raman bands could be attributed to the Raman mode, involving motions of the Fe^{3+} cations. However, the Raman spectra for the Duplex magnesioferrite indicate moderate right shifting for the bands at ≈700–710 and 200–210 cm^{-1}, depending on increases in CuO content. Moreover, the spectrum of magnesioferitte with 16.8 wt % CuO shows additional weak band at 596 ($F_{2g}3$) cm^{-1} and very weak shoulder at ≈660–670 ($A_{1g}1$) cm^{-1}, which seem to be very distinctive for inverse spinel structure [40,41].

It is noteworthy that many ferrite spinels present complete or partial inverse structure, in which the A^{2+} cations may occupy the M sites and the Fe^{3+} cations are distributed between the T and M sites [39]. For example, some magnetite grains have a complete inverse spinel structure. Depending on synthesis conditions, the inversion degree in cubic $CuFe_2O_4$ varies from 0.1 to 1.0 [27,32,34]. Among Cu-containing ferrite spinel, the Raman spectra was measured only for tetragonal $CuFe_2O_4$ [37] and a series of cubic $Mg_{0.5}Zn_{0.5}Fe_2O_4$–$Mg_{0.5}Cu_{0.5}Fe_2O_4$ [36,38]. The latter compound is very close in composition and Raman bands to the Duplex magnesioferrite with maximal CuO content (17.3 wt %).

Therefore, we can suggest that the incorporation of Cu due to the $Mg^{2+} \leftrightarrow Cu^{2+}$ isomorphism is to increase the inversion degree in the Duplex magnesioferrite structure.

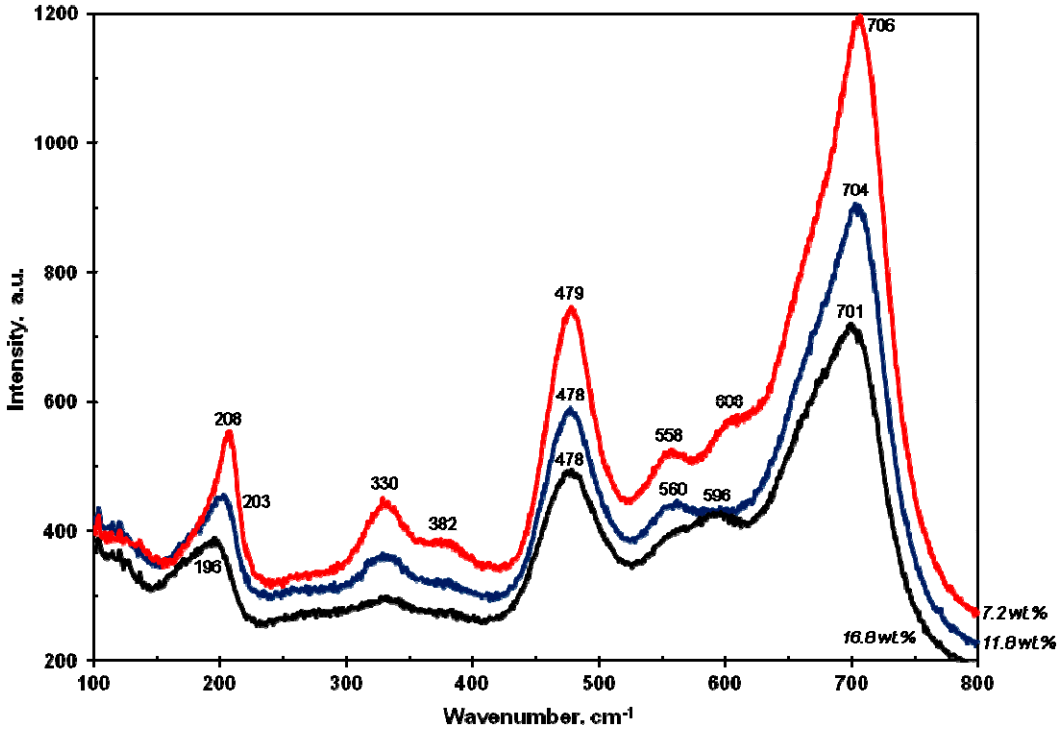

Figure 11. Unoriented Raman spectra for magnesioferrite with different CuO content from the Duplex lava tube, Tolbachik volcano, Kamchatka peninsula, Russia.

7. Discussion and Final Remarks

Chloride crusts covering walls and fractures in the Duplex lava tube and associated mineral assemblages of Cu-bearing magnesioferrite, hematite, and high-Ca silicates in the outer rim of the lava substrate may assist in deciphering the compositions and processes in shallow volcanic plumbing systems (e.g., precipitation from gas phase and gas-rock interaction). In general, the appearance of hematite and other Fe^{3+}-oxides due to the gas-rock interaction is common in many vesicular types of lava [42] and in combustion metamorphism systems. The high-temperature silicate assemblages, which sometimes occur with esseneite, melilite, spinel, and/or hematite, are typical of pyrogenic transformations of some sedimentary rocks into paralava: natural fires of coal and other caustobioliths and burning in coal mines dumps [43–49]. Such processes are always associated with fumarole activity.

The recorded Cu-bearing magnesioferrite in close association with tenorite and hematite is analogous with modern base metal smelters, which operate at high temperatures and oxygen fugacity at atmospheric pressure. Cuprospinel, delafossite ($CuFeO_2$), tenorite, and Fe-silicates are common products of oxidative combustion of copper sulfides, hematite, quartz, and K-silicates, along with an added silica flux at the Olympic Dam copper smelter [2]. Similarly, cuprospinel and other Cu–Mg ferrite spinels also formed in ignited Cu–Zn ore dumps in Newfoundland, where high-temperature roasting was caused by oxidation involving Mg-silicates [1].

In the case of the Duplex lava tube, we propose that such "chemical" roasting at low pressure and high oxygen fugacity was caused by periodic bursts of high-temperature gas through the lava tubes. High (nearly magmatic) temperature of the gaseous media was independently confirmed by direct measurements of venting gases in skylights and lava fractures and lava melting in the tube roof [11,13]. We do not exclude that the early fumarole products (chlorides and sulfates) near skylights may involve gas-wallrock interaction. The chloride component in oxidized gas can be a powerful flux and leaching agent, which affected surrounding basaltic rocks and accumulated Cu, Zn, and other elements.

The mineral relations within reactionary zones and vesicles suggests that the following crystallization sequence occurred [2]: Ca-rich silicates + Ti-rich hematite ± Cu-free magnesioferrite →

Cu-containing hematite → Cu-rich magnesioferrite → tenorite → gold → halite + sylvite ± Na-K-, K-Cu-, Cu-chlorides/oxychlorides (Figure 7, Figure 8 and Figure S2). This assumes gradual decreasing of Fe and increasing of Cu (at the stage of Fe–Cu-oxides crystallization) and then abrupt decreases in Cu after the tenorite formation. The absence of delafossite ($CuFeO_2$), an oxide mineral containing Cu^{1+} and Fe^{3+}, indicates very high oxidation conditions of crystallization in the studied Duplex assemblages with Cu^{2+}-dominant oxides. The sulfate component does not appear to participate in this gas-rock interaction, and may instead be precipitated as other Cu-bearing sulfates in nearby fumaroles (e.g., Saranchinaitovaya fumarole, Naboko scoria cone). The crystallization temperatures of the Duplex Fe-Cu-oxides were undoubtedly very high (800–1000 °C). According to experimental data [26,28], the association of hematite + cuprospinel + tenorite is most stable in this temperature interval. Unlike the Duplex associations, the temperature interval for crystallization of Cu-rich oxide spinels in the Arsenatnaya and other Tolbachik fumaroles is suggested to be 600–800 °C [4,5,16].

In general, exhalation assemblages from the Duplex lava tube are comparable with those from high-temperature areas in fumaroles of the Second scoria cone of the 1975 Northern Breakthrough. However, these unique fumaroles (Arsenatnaya, Yadovitaya) are long-living systems, in which various minerals, including Cu^{2+}-dominant species, precipitated directly from the gas phase as volcanic sublimates, or were formed as a result of gas-rock interaction in fumarole chambers, where the host basalt was the source of the less volatile elements as Al, Ti, Mg, and Ca [4,5]. In contrast, the Duplex associations are high-temperature products of short-term interactions of gas with host trachyandesites. In this case the gas phase cannot be saturated by many elements, like in fumaroles of the Second scoria cone of the 1975 Northern Breakthrough.

Supplementary Materials: The supplementary Tables S1–S6 and Figures S1 and S2 are available at http://www.mdpi.com/2075-163X/8/11/514/s1.

Author Contributions: V.V.S., V.S.K., and A.B.B. wrote the paper. V.V.S. performed the mineralogical description, measurements of chemical composition and Raman studies of Cu-rich magnesioferrite and related minerals. V.S.K. and L.M.Z. provided preliminary SEM studies. L.M.Z. helped in collection and selection of samples. A.A. provided the native English of the manuscript and formula calculations of minerals.

Funding: The field work and sample collection was partly supported by RFBR (grant 16-05-00945a) and the State assignment projects (0330-2016-0001, 0330-2016-0005). The investigations were funded by the Russian Science Foundation (grant 16-17-10145).

Acknowledgments: The authors would like to thank Elena N. Nigmatulina, Nikolay S. Karmanov, and Mikhail V. Khlestov for technical assistance at EMPA and SEM studies. Maya B. Kamenetsky, Dmitry P. Savelyev, Kirill I. Shmulovich, Marina G. Belousova, Sergey M. Zakharov, and Igor V. Pekov are thanked for good advice and sharing their expertise and data.

Conflicts of Interest: The authors declare no conflict of interest.

References

1. Nickel, E.H. The new mineral cuprospinel ($CuFe_2O_4$) and other spinels from an oxidized ore dump at Baie Verte, Newfoundland. *Can. Mineral.* **1973**, *11*, 1003–1007.
2. Kamenetsky, V.S.; Belousov, A.; Sharygin, V.V.; Zhitova, L.M.; Ehrig, K.; Zelenski, M.E.; Chaplygin, I.; Yudovskaya, M.A.; Nesterenko, P.N.; Zakharov, S.M. Natural gold-copper smelting with chloride flux in lava tubes of Tolbachik volcano (Kamchatka arc). *Geochem. Perspect. Lett.* **2018**, submitted.
3. Pekov, I.V.; Agakhanov, A.A.; Zubkova, N.V.; Koshlyakova, N.N.; Shchipalkina, N.V.; Sandalov, F.D.; Yapaskurt, V.O.; Turchkova, A.G.; Sidorov, E.G. *High fO_2 Volcanic Exhalation Systems with Exceptional Mineralogy and Chemistry*; Abstracts of International Conference Dedicated to the 110th Anniversary of Academician V.S. Sobolev "The Problems of Magmatic and Metamorphic Petrology, Geodynamics and Genesis of Diamonds", IGM SD RAS; Publishing House of SB RAS: Novosibirsk, Russia, 2018; p. 146.
4. Pekov, I.V.; Koshlyakova, N.N.; Zubkova, N.V.; Lykova, I.S.; Britvin, S.N.; Yapaskurt, V.O.; Agakhanov, A.A.; Shchipalkina, N.V.; Turchkova, A.G.; Sidorov, E.G. Fumarolic arsenates—A special type of arsenic mineralization. *Eur. J. Mineral.* **2018**, *30*, 305–322. [CrossRef]

5. Pekov, I.V.; Sandalov, F.D.; Koshlyakova, N.N.; Polekhovsky, Y.S.; Vigasina, M.F.; Britvin, S.N.; Sidorov, E.G.; Turchkova, A.G. Copper in natural oxide spinels: The new mineral thermaerogenite $CuAl_2O_4$, cuprospinel and Cu-enriched varieties of other spinel-group members from fumaroles of the Tolbachik Volcano, Kamchatka, Russia. *Minerals* **2018**, *8*, 498. [CrossRef]
6. Biagioni, C.; Pasero, M. The systematics of the spinel-type minerals: An overview. *Am. Mineral.* **2014**, *99*, 1254–1264. [CrossRef]
7. Belousov, A.; Belousova, M.; Edwards, B.; Volynets, A.; Melnikov, D. Overview of the precursors and dynamics of the 2012–13 basaltic fissure eruption of Tolbachik Volcano, Kamchatka, Russia. *J. Volcanol. Geotherm. Res.* **2015**, *307*, 22–37. [CrossRef]
8. Belousov, A.; Belousova, M. Dynamics and viscosity of 'a'a and pahoehoe lava flows of the 2012–2013 eruption of Tolbachik volcano, Kamchatka (Russia). *Bull. Volcanol.* **2018**, *80*, 6. [CrossRef]
9. Volynets, A.O.; Edwards, B.R.; Melnikov, D.; Yakushev, A.; Griboedova, I. Monitoring of the volcanic rock compositions during the 2012–2013 fissure eruption at Tolbachik volcano, Kamchatka. *J. Volcanol. Geotherm. Res.* **2015**, *307*, 120–132. [CrossRef]
10. Zelenski, M.; Malik, N.; Taran, Y. Emissions of trace elements during the 2012–2013 effusive eruption of Tolbachik volcano, Kamchatka: Enrichment factors, partition coefficients and aerosol contribution. *J. Volcanol. Geotherm. Res.* **2014**, *285*, 136–149. [CrossRef]
11. Chaplygin, I.V.; Lavrushin, V.Y.; Dubinina, E.O.; Bychkova, Y.V.; Inguaggiato, S.; Yudovskaya, M.A. Geochemistry of volcanic gas at the 2012–13 New Tolbachik eruption, Kamchatka. *J. Volcanol. Geotherm. Res.* **2016**, *323*, 186–193. [CrossRef]
12. Chaplygin, I.; Yudovskaya, M.; Vergasova, L.; Mokhov, A. Native gold from volcanic gases at Tolbachik 1975–76 and 2012–13 fissure eruptions, Kamchatka. *J. Volcanol. Geotherm. Res.* **2015**, *307*, 200–209. [CrossRef]
13. Zelenski, M.; Kamenetsky, V.S.; Hedenquist, J. Gold recycling and enrichment beneath volcanoes: A case study of Tolbachik, Kamchatka. *Earth Planet. Sci. Lett.* **2016**, *437*, 35–46. [CrossRef]
14. Karpov, G.A.; Krivovichev, S.V.; Vergasova, L.P.; Chernyat'eva, A.P.; Anikin, L.P.; Moskaleva, S.V.; Filatov, S.K. Oxysulfates of copper, sodium, and potassium in the lava flows of the 2012–2013 Tolbachik Fissure Eruption. *J. Volcanol. Seismol.* **2013**, *7*, 362–370. [CrossRef]
15. Filatov, S.K.; Shablinskii, A.P.; Vergasova, L.P.; Saprikina, O.Y.; Bubnova, R.S.; Moskaleva, S.V.; Belousov, A.B. Belomarinaite, IMA 2017-069a. CNMNC Newsletter No. 43, June 2018, page 781. *Mineral. Mag.* **2018**, *82*, 779–785. [CrossRef]
16. Pekov, I.V.; Zubkova, N.V.; Yapaskurt, V.O.; Belakovskiy, D.I.; Chukanov, N.V.; Lykova, I.S.; Saveliev, D.P.; Sidorov, E.G.; Pushcharovsky, D.Y. Wulffite, $K_3NaCu_4O_2(SO_4)_4$, and parawulffite, $K_5Na_3Cu_8O_4(SO_4)_8$, two new minerals from fumarole sublimates of the Tolbachik volcano, Kamchatka, Russia. *Can. Mineral.* **2014**, *52*, 699–716. [CrossRef]
17. Nazarchuk, E.V.; Siidra, O.I.; Agakhanov, A.A.; Lukina, E.A.; Avdontseva, E.Y.; Karpov, G.A. Itelmenite, $Na_2CuMg_2(SO_4)_4$, a new anhydrous sulphate mineral from the Tolbachik volcano. *Mineral. Mag.* **2018**, *82*. [CrossRef]
18. Filatov, S.K.; Karpov, G.A.; Shablinskii, A.P.; Krivovichev, S.V.; Vergasova, L.P.; Antonov, A.V. Ivsite, $Na_3H(SO_4)_2$, a new mineral from volcanic exhalations of fumaroles of the fissure Tolbachik eruption of the 50th anniversary of the Institute of Volcanology and Seismology, Far East Branch, Russian Academy of Sciences. *Dokl. Earth. Sci.* **2016**, *468*, 632–635. [CrossRef]
19. Gorelova, L.A.; Vergasova, L.P.; Krivovichev, S.V.; Avdontseva, E.Y.; Moskaleva, S.V.; Karpov, G.A.; Filatov, S.K. Bubnovaite, $K_2Na_8Ca(SO_4)_6$, a new mineral species with modular structure from the Tolbachik volcano, Kamchatka peninsula, Russia. *Eur. J. Mineral.* **2016**, *28*, 677–686. [CrossRef]
20. Siidra, O.I.; Nazarchuk, E.V.; Agakhanov, A.A.; Lukina, E.A.; Zaitsev, A.N.; Turner, R.; Filatov, S.K.; Pekov, I.V.; Karpov, G.A.; Yapaskurt, V.O. Hermannjahnite, $CuZn(SO_4)_2$, a new mineral with chalcocyanite derivative structure from the Naboko scoria cone of the 2012–2013 fissure eruption at Tolbachik volcano, Kamchatka, Russia. *Mineral. Petrol.* **2018**, *112*, 123–134. [CrossRef]
21. Siidra, O.I.; Lukina, E.A.; Nazarchuk, E.V.; Depmeier, W.; Bubnova, R.S.; Agakhanov, A.A.; Avdontseva, E.Y.; Filatov, S.K.; Kovrugin, V.M. Saranchinaite, $Na_2Cu(SO_4)_2$, a new exhalative mineral from Tolbachik volcano, Kamchatka, Russia, and a product of the reversible dehydration of kröhnkite, $Na_2Cu(SO_4)_2(H_2O)_2$. *Mineral. Mag.* **2018**, *82*, 257–274. [CrossRef]

22. Pouchou, I.L.; Pichoir, F. "PaP" (phi-rho-z) procedure for improved quantitative microanalysis. In *Microbeam Analysis*; Armstrong, I.T., Ed.; San Francisco Press: San Francisco, CA, USA, 1985; pp. 104–106.
23. Plechov, P.; Blundy, J.; Nekrylov, N.; Melekhova, E.; Shcherbakov, V.; Tikhonova, M.S. Petrology and volatile content of magmas erupted from Tolbachik Volcano, Kamchatka, 2012–13. *J. Volcanol. Geotherm. Res.* **2015**, *307*, 182–199. [CrossRef]
24. Shcherbakov, V.D.; Plechov, P.Y. P-bearing olivine from lava flow of 2012–2013 Tolbachik volcano eruption. *New Data Miner.* **2018**, *52*, 15–17.
25. Antoshina, L.G.; Goryaga, A.N.; Kamzolov, E.A.; Kukudzhanova, E.N. Nature of low-temperature transitions in $CuFe_2O_4$ ferrite. *J. Exp. Theor. Phys.* **1996**, *83*, 1149–1151.
26. Ristić, M.; Hannoyer, B.; Popović, S.; Musić, S.; Bajraktaraj, N. Ferritization of copper ions in the Cu-Fe-O system. *Mater. Sci. Eng. B Solid State Mater. Adv. Technol.* **2000**, *B77*, 73–82. [CrossRef]
27. Lakhani, V.K.; Pathak, T.K.; Vasoya, N.H.; Modi, K.B. Structural parameters and X-ray Debye temperature determination study on copper ferrite-aluminates. *Solid State Sci.* **2011**, *13*, 539–547. [CrossRef]
28. Marinca, T.F.; Chicinaş, I.; Isnard, O. Influence of the heat treatment conditions on the formation of $CuFe_2O_4$ from mechanical milled precursors oxides. *J. Therm. Anal. Calorim.* **2012**, *110*, 301–307. [CrossRef]
29. Balagurov, A.M.; Bobrikov, I.A.; Maschenko, M.S.; Sangaa, D.; Simkin, V.G. Structural phase transition in $CuFe_2O_4$ spinel. *Crystallogr. Rep.* **2013**, *58*, 710–717. [CrossRef]
30. Ateia, E.; Ahmed, M.A.; Ghouniem, R.M. Electrical properties and initial permeability of Cu-Mg ferrites. *Solid State Sci.* **2014**, *31*, 99–106. [CrossRef]
31. Köferstein, R.; Walther, T.; Hesse, D.; Ebbinghaus, S.G. Crystallite-growth, phase transition, magnetic properties, and sintering behavior of nano-$CuFe_2O_4$ powders prepared by a combustion-like process. *J. Solid State Chem.* **2014**, *213*, 57–64. [CrossRef]
32. Kyono, A.; Gramsch, S.A.; Nakamoto, Y.; Sakata, M.; Kato, M.; Tamura, T.; Yamanaka, T. High-pressure behavior of cuprospinel $CuFe_2O_4$: Influence of the Jahn-Teller effect on the spinel structure. *Am. Mineral.* **2015**, *100*, 1752–1761. [CrossRef]
33. Rashad, M.M.; Soltan, S.; Ramadan, A.A.; Bekheet, M.F.; Rayan, D.A. Investigation of the structural, optical and magnetic properties of $CuO/CuFe_2O_4$ nanocomposites synthesized via simple microemulsion method. *Ceram. Int.* **2015**, *41*, 12237–12245. [CrossRef]
34. Agouriane, E.; Rabi, B.; Essoumhi, A.; Razouk, A.; Sahlaoui, M.; Costa, B.F.O.; Sajieddine, M. Structural and magnetic properties of $CuFe_2O_4$ ferrite nanoparticles synthesized by co-precipitation. *J. Mater. Environ. Sci.* **2016**, *7*, 4116–4120.
35. Kongkaew, T.; Sakurai, K. Low-temperature synthesis of cubic phase $CuFe_2O_4$ powder. *Chem. Lett.* **2017**, *46*, 1493–1496. [CrossRef]
36. Yadav, A.; ·Varshney, D. Structural and dielectric properties of copper-substituted Mg–Zn spinel ferrites. *J. Supercond. Nov. Magn.* **2017**, *30*, 1297–1302. [CrossRef]
37. Le Nestour, A.; Gaudon, M.; Villeneuve, G.; Andriessen, R.; Demourgues, A. Steric and electronic effects relating to the Cu^{2+} Jahn-Teller distortion in $Zn_{1-x}Cu_xAl_2O_4$ spinels. *Inorg. Chem.* **2007**, *46*, 2645–2658. [CrossRef] [PubMed]
38. Verma, K.; Kumar, A.; Varshney, D. Effect of Zn and Mg doping on structural, dielectric and magnetic properties of tetragonal $CuFe_2O_4$. *Curr. Appl. Phys.* **2013**, *13*, 467–473. [CrossRef]
39. D'Ippolito, V.; Andreozzi, G.B.; Bersani, D.; Lottici, P.P. Raman fingerprint of chromate, aluminate and ferrite spinels. *J. Raman Spectr.* **2015**, *46*, 1255–1264. [CrossRef]
40. Nakagomi, F.; da Silva, S.W.; Garg, V.K.; Oliveira, A.C.; Morais, P.C.; Franco, A., Jr. Influence of the Mg-content on the cation distribution in cubic $Mg_xFe_{3-x}O_4$ nanoparticles. *J. Solid State Chem.* **2009**, *182*, 2423–2429. [CrossRef]
41. Da Silva, S.W.; Nakagomi, F.; Silva, M.S.; Franco, A., Jr.; Garg, V.K.; Oliveira, A.C.; Morais, P.C. Raman study of cations' distribution in $Zn_xMg_{1-x}Fe_2O_4$ nanoparticles. *J. Nanopart. Res.* **2012**, *14*, 798. [CrossRef]
42. Xu, H.; Lee, S.; Xu, H. Luogufengite: A new nano-mineral of Fe_2O_3 polymorph with giant coercive field. *Am. Mineral.* **2017**, *102*, 711–719. [CrossRef]
43. Cosca, M.A.; Peacor, D.R. Chemistry and structure of esseneite ($CaFe^{3+}AlSiO_6$), a new pyroxene produced by pyrometamorphism. *Am. Mineral.* **1987**, *72*, 148–156.
44. Chesnokov, B.V.; Shcherbakova, E.P. *The Mineralogy of Burned Heaps in the Chelyabinsk Coal Basin*; Publ. H. Nauka: Moscow, Russia, 1991; 152p. (In Russian)

45. Sokol, E.V.; Maksimova, N.V.; Nigmatulina, E.N.; Sharygin, V.V.; Kalugin, V.M. *Combustion Metamorphism*; Publ. H. SB RAS: Novosibirsk, Russia, 2005; 284p. (In Russian)
46. Sokol, E.V.; Novikov, I.S.; Vapnik, Y.; Sharygin, V.V. Gas fire from mud volcanoes as a trigger for the appearance of high-temperature pyrometamorphic rocks of the Hatrurim Formation (Dead Sea area). *Dokl. Earth Sci.* **2007**, *413*, 474–480. [CrossRef]
47. Vapnik, Y.; Sharygin, V.V.; Sokol, E.V.; Shagam, R. Paralavas in combustion metamorphic complex at the Hatrurim Basin, Israel. In *Geology of Coal Fires: Case Studies from Around the World*; Stracher, G., Ed.; Geological Society of America: Boulder, CO, USA, 2007; pp. 133–153.
48. Sharygin, V.V.; Sokol, E.V.; Belakovskii, D.I. Fayalite-sekaninaite paralava from the Ravat coal fire (central Tajikistan). *Russ. Geol. Geophys.* **2009**, *50*, 703–721. [CrossRef]
49. Sharygin, V.V. Mayenite-supergroup minerals from burned dump of the Chelyabinsk coal basin. *Russ. Geol. Geophys.* **2015**, *56*, 1603–1621. [CrossRef]